

Piezoresistivity and Strain-induced Band Gap Tuning in Atomically Thin MoS₂

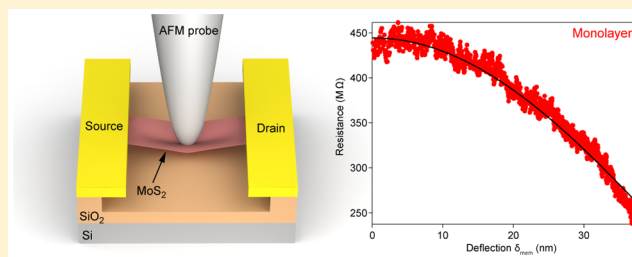
Sajede Manzeli, Adrien Allain, Amirhossein Ghadimi, and Andras Kis*

Electrical Engineering Institute, École Polytechnique Fédérale de Lausanne (EPFL), CH-1015 Lausanne, Switzerland

S Supporting Information

ABSTRACT: Continuous tuning of material properties is highly desirable for a wide range of applications, with strain engineering being an interesting way of achieving it. The tuning range, however, is limited in conventional bulk materials that can suffer from plasticity and low fracture limit due to the presence of defects and dislocations. Atomically thin membranes such as MoS₂ on the other hand exhibit high Young's modulus and fracture strength, which makes them viable candidates for modifying their properties via strain. The bandgap of MoS₂ is highly strain-tunable, which results in the modulation of its electrical conductivity and manifests itself as the piezoresistive effect, whereas a piezoelectric effect was also observed in odd-layered MoS₂ with broken inversion symmetry. This coupling between electrical and mechanical properties makes MoS₂ a very promising material for nanoelectromechanical systems (NEMS). Here, we incorporate monolayer, bilayer, and trilayer MoS₂ in a nanoelectromechanical membrane configuration. We detect strain-induced band gap tuning via electrical conductivity measurements and demonstrate the emergence of the piezoresistive effect in MoS₂. Finite element method (FEM) simulations are used to quantify the band gap change and to obtain a comprehensive picture of the spatially varying bandgap profile on the membrane. The piezoresistive gauge factor is calculated to be -148 ± 19 , -224 ± 19 , and -43.5 ± 11 for monolayer, bilayer, and trilayer MoS₂, respectively, which is comparable to state-of-the-art silicon strain sensors and 2 orders of magnitude higher than in strain sensors based on suspended graphene. Controllable modulation of resistivity in 2D nanomaterials using strain-induced bandgap tuning offers a novel approach for implementing an important class of NEMS transducers, flexible and wearable electronics, tunable photovoltaics, and photodetection.

KEYWORDS: two-dimensional materials, MoS₂, band gap engineering, piezoresistivity, NEMS, nanoelectromechanical measurements



MoS₂ consists of vertically stacked, weakly interacting layers held together by van der Waals interaction and is a typical material from the transition metal dichalcogenide (TMDC) family.¹ Although few-layer TMDCs are indirect bandgap semiconductors, they become direct gap semiconductors in their monolayer form.^{2–6} The demonstration of the first monolayer MoS₂-based transistor⁷ opened the way to fundamental studies and practical applications based on electrical transport in mesoscopic TMDC and enabled fabrication of high performance electronic and optoelectronic devices based on these materials.⁸ From the mechanical point of view, MoS₂ benefits from its atomic-scale thickness, ultralow weight and low intrinsic mechanical dissipation making it interesting for the realization of nanoresonators.⁹ It has a high Young's modulus of ~ 270 GPa¹⁰ and can sustain in-plane strain levels as high as 11%,¹⁰ which puts it in the category of ultrastrong materials.¹⁰ It can also avoid inelastic relaxation due to its high elastic strain limit.¹¹ All these features make MoS₂ and other TMDCs in general interesting for strain engineering and have motivated numerous theoretical studies,^{12–17} showing, for example, that under small compressive strains ($<2\%$) the bandgap is expected to increase.¹⁷ Under tensile strain, the bandgap of monolayer and bilayer MoS₂ should be reduced and result in a

semiconductor to metal transition for strain levels as high as 10% for monolayer and 6% for bilayer MoS₂.^{16–19} Moreover, in the case of monolayer MoS₂, the indirect gap is only slightly higher in energy compared to the direct gap^{17,20} and is more sensitive to strain, thus direct to indirect gap transition is expected under moderate strains.^{13,17,18} The strain induced bandgap modulation gives rise to a piezoresistive effect, in which a change in resistivity of the material is observed during mechanical deformation, as was previously reported in the case of bilayer MoS₂ deposited on flexible substrates.²¹ In addition to piezoresistivity, odd-layered ultrathin MoS₂ was also shown to exhibit the piezoelectric effect.^{21,22}

Although experimental reports on the strain-induced modification of the bandgap under tensile strain¹² and inhomogeneous local strain²³ have been published, they all relied on optical measurements. He et al. reported an exciton redshift at a rate of ~ 70 meV/% strain for single-layer and at a larger rate for bilayer MoS₂.¹² Raman spectroscopy revealed the effect of strain on the vibrational modes and the strain-induced

Received: April 29, 2015

Revised: July 9, 2015

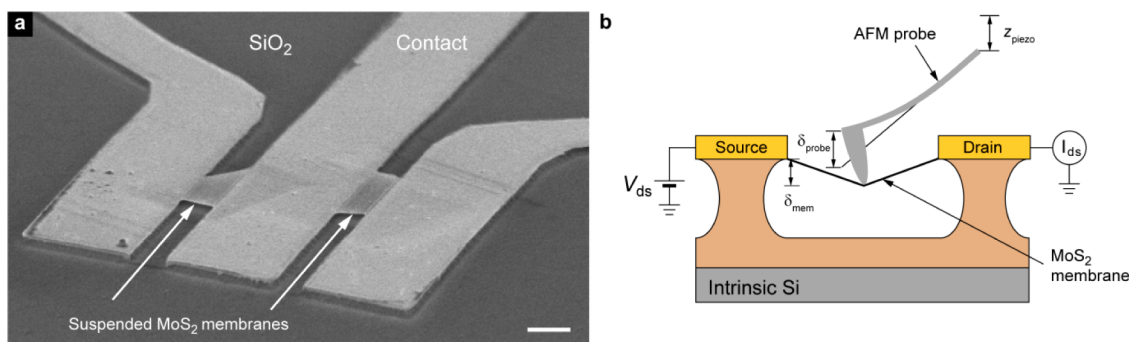


Figure 1. Suspended MoS₂ devices and the measurement setup. (a) Scanning electron microscope (SEM) image of typical MoS₂ devices with suspended channels and contact electrodes. Scale bar is 1 μm . (b) Schematic drawing of the setup for direct current electrical characterization of suspended channel MoS₂ devices under strain. The suspended atomically thin membrane is deformed at the center using an AFM probe attached to a piezo scanner. The vertical displacement of the scanner (z_{piezo}) results in the deflection of the cantilever (δ_{probe}) and the membrane (δ_{mem}). The device is kept under bias voltage V_{ds} whereas the drain current I_{ds} is monitored.

symmetry breaking.²⁴ Local strain engineering was also shown to result in the funnel effect.²³ The use of photoluminescence spectroscopy in most of these studies, however, restricts these studies to mono- and bilayer MoS₂, and there is a lack of experimental information on the influence of strain-induced bandgap changes on electrical properties of MoS₂, which is needed to assess the potential of this class of materials as building blocks for NEMS devices such as self-sensing resonators or strain sensors.²⁵

Here, we investigate the effect of mechanical strain on the electrical conductivity of suspended MoS₂ membranes. We apply mechanical strain using an atomic force microscope tip while simultaneously carrying out electrical measurements, allowing us to detect the strain-induced bandgap modulation through its influence on the electrical conductivity. The device fabrication starts by mechanical exfoliation of mono-, bi-, and trilayer MoS₂ onto intrinsic, undoped Si substrates covered with a 270 nm thick SiO₂ layer. The use of intrinsic Si and the absence of gate electrodes minimizes the effect of capacitive coupling between the MoS₂ membrane and the substrate. Electrodes are fabricated using standard e-beam lithography and the 2D semiconductor is suspended by etching away a portion of the underlying SiO₂. Figure 1a shows a typical suspended MoS₂ device made from a single MoS₂ flake with electrical contacts clamping the suspended membrane.

In order to probe the electromechanical response of the suspended MoS₂ membrane, after the MoS₂ membrane is imaged and located using AFM in the AC mode, we position the AFM tip in the center of the membrane and deform it while applying a DC bias voltage (V_{ds}) between source and drain contacts. The drain current (I_{ds}) and membrane deformation δ_{mem} are recorded in situ in a setup schematically depicted in Figure 1b. During a nanoindentation measurement, the piezoscanner displaces the AFM probe in the vertical direction with a controlled speed. Figure 2a shows the electrical response to the nanoindentation of device 1 (monolayer, see Supporting Information Section 3). The tip of the probe touches the membrane and starts to deform it, resulting in increasing deflection of the AFM probe δ_{probe} . Once a predefined deflection is attained, the probe is retracted. At the same time, we record the drain current (I_{ds}) under a bias voltage ($V_{\text{ds}} = 200 \text{ mV}$), shown in the lower panel of Figure 2a. Both the electrical and mechanical response are reproducible over extension and retraction cycles of the AFM piezo scanner motion, indicating that the membrane is deformed in the elastic regime and that there is no slippage of

the membrane under the metal contacts (Supporting Information Figure S7). In addition, the reproducibility of current measurements shows that the contact interface between MoS₂ and the electrodes is not degraded during the nanoelectromechanical testing.

Concurrent measurements of the current and tip deflection allow us to observe the effect of deformation and confirm the mechanical origin of the current modulation. In the case of measurements on the monolayer MoS₂ device presented on Figure 2a, while the membrane is in the relaxed state, the current remains at a constant value of 470 pA. It starts to increase as soon as the membrane begins to deform, reaching a value of $\sim 800 \text{ pA}$ at maximum deformation. During the probe retraction cycle, current follows the opposite trend and returns to its predeformation value as the tip is fully retracted. The deflection of the membrane δ_{mem} at the center (right under the AFM tip) is related to the probe deflection δ_{probe} and vertical position of the piezoscanner z_{piezo} by $z_{\text{piezo}} = \delta_{\text{mem}} + \delta_{\text{probe}}$ ²⁶ (Figure 1b). This allows us to plot the current I_{ds} as a function of δ_{mem} in Figure 2b. As shown in Figure 2b, the current I_{ds} increases with the increased deformation of the membrane, indicating the modulation of resistance due to the applied deformation.

In a different set of measurements, the output characteristics of the device is compared in the relaxed state and under constant deformation (Figure 2c). The current is systematically higher under a deformation of $\delta_{\text{mem}} = 33 \text{ nm}$ than in the absence of deformation (black curve). Both curves are linear and symmetric, indicating that the piezotronic effect²¹ due to a change in Schottky barrier height by piezoelectric polarization charges is negligible in this case and that the device response is dominated by the piezoresistive effect.

We have performed the same set of electromechanical measurements on six monolayer, three bilayer, and three trilayer MoS₂ devices of various widths (85 nm–6 μm), lengths (570 nm–1.4 μm) and aspect ratios (length/width = 0.17–13), presented in Supporting Information Section 3. In all cases, we eventually deformed the MoS₂ membrane up to mechanical failure (Supporting Information Figure S4) with the current increasing with increasing deformation in all the cases.

This observed piezoresistive behavior can be understood in terms of band gap reduction under tensile strain.^{12,13,23} In the subthreshold regime and at room temperature, thermally activated transport dominates and the electrical current is

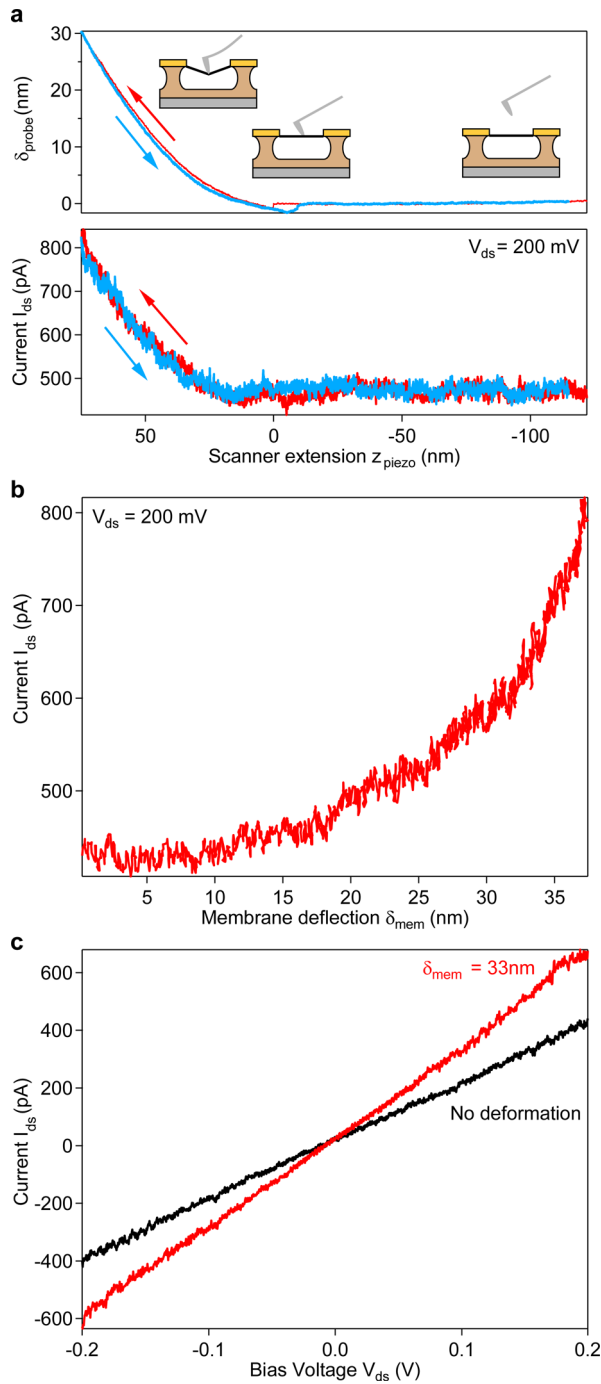


Figure 2. Piezoresistive response of a monolayer MoS₂ nanoelectromechanical device. (a) Output data from electromechanical experiment on device 1 showing simultaneous measurement of the cantilever deflection (top panel) and the drain current (bottom panel) as a function of the piezo scanner extension. The electromechanical response is reproducible in both extension (red) and retraction (blue) cycles. (b) Drain current as a function of membrane deflection at the center $\delta_{\text{mem}} = (z_{\text{piezo}} - \delta_{\text{probe}})$. (c) Output characteristics of the same MoS₂ device. The black curve is recorded after the AFM tip has touched the membrane and before indentation. The red curve is recorded while the membrane is kept at constant deformation. The modulation of carrier transport under strain is consistent with the extension and retraction experiments in panel a and the piezoresistive effect.

carried by electrons thermally excited into the conduction band. The conductivity is then expressed as²⁷

$$\sigma = \sigma_0 \exp \left[-\frac{E_C - E_F}{k_B T} \right] \quad (1)$$

where σ_0 is the minimum conductivity defined by the hopping distance, E_C is the conduction band edge, E_F is the Fermi energy, k_B is the Boltzmann constant, and T the temperature. Assuming a symmetric reduction of bandgap under strain,^{17,23,28–32} the conduction band would be shifted to lower energies while the valence band edge would be shifted to higher energies by the same amount. For small strains (up to 7% in our case), the bandgap is expected to change linearly with strain^{12,17,18,30,33} and the conductivity can be written as (see Supporting Information Section 5 for derivation)

$$\sigma_{\text{def}} = \sigma_{\text{rel}} \exp \left[-\frac{\epsilon}{2k_B T} \frac{\partial E_g}{\partial \epsilon} \right] \quad (2)$$

σ_{def} and σ_{rel} are the conductance of the membrane in the deformed and relaxed state, respectively, ϵ is strain, and $\partial E_g / \partial \epsilon$ is the rate of bandgap change with strain. For negative values of $\partial E_g / \partial \epsilon$, eq 2 predicts increasing conductivity.

The strain distribution induced in our MoS₂ membranes during the nanoindentation experiment is however not uniform, motivating the use of finite element modeling (FEM) for extracting the rate of band gap change $\partial E_g / \partial \epsilon$ from our measurements. Figure 3a shows an AFM image of an electromechanical device based on a suspended trilayer MoS₂ membrane (device 11, see Supporting Information Section 3). Using FEM, we calculate the total conductance of the membrane as a function of δ_{mem} for a range of $\partial E_g / \partial \epsilon$ and different values of contact resistance R_C . Figure 3b shows simulated resistance as a function of membrane deflection for $\partial E_g / \partial \epsilon$ in the range between 0 and -100 meV/% strain and $R_C = 2$ M Ω . Comparing simulations and measurement results, it is possible to select among the simulated values of $\partial E_g / \partial \epsilon$ and R_C a pair of parameters that gives the smallest sum of the squared difference between the observed and simulated values, resulting in this particular case in $\partial E_g / \partial \epsilon = -21$ meV/% strain and $R_C = 2$ M Ω . The extracted value of contact resistance is in line with previously reported values³⁴ and corresponds to $\sim 8\%$ of the total device resistance in its relaxed state. Because our devices are in the sub-threshold regime due to the absence of gating, the resistance of the semiconducting channel is dominant, and thus, the piezoresistive behavior of the channel is not masked by the effect of the in-series contact resistance.

In Figure 3c, we show FEM simulation of the spatial distribution of bandgap change ΔE_g under an inhomogeneous strain resulting from a membrane deformation at midpoint equal to $\delta_{\text{mem}} = 75$ nm. A spatially inhomogeneous strain field generates a spatially varying bandgap in an initially homogeneous atomically thin membrane. The profile of the bandgap change ΔE_g along the dashed line in Figure 3c is shown in Figure 3d, indicating that areas near the tip are experiencing more deflection and thus more strain and the largest change of band gap.

Measured and simulated curves for representative mono-, bi-, and trilayer devices (samples 1, 7, and 11; see Supporting Information Section 3) are shown on Figure 4a–c.

Figure 4d depicts the calculated $|\partial E_g / \partial \epsilon|$ for all devices (for the geometry of each device see Supporting Information Section 3). The error bars are calculated considering the uncertainty on the input parameters. We find that the bandgap is being tuned at rates of -77.3 ± 10 meV/% strain, -116.7 ± 10 meV/% strain,

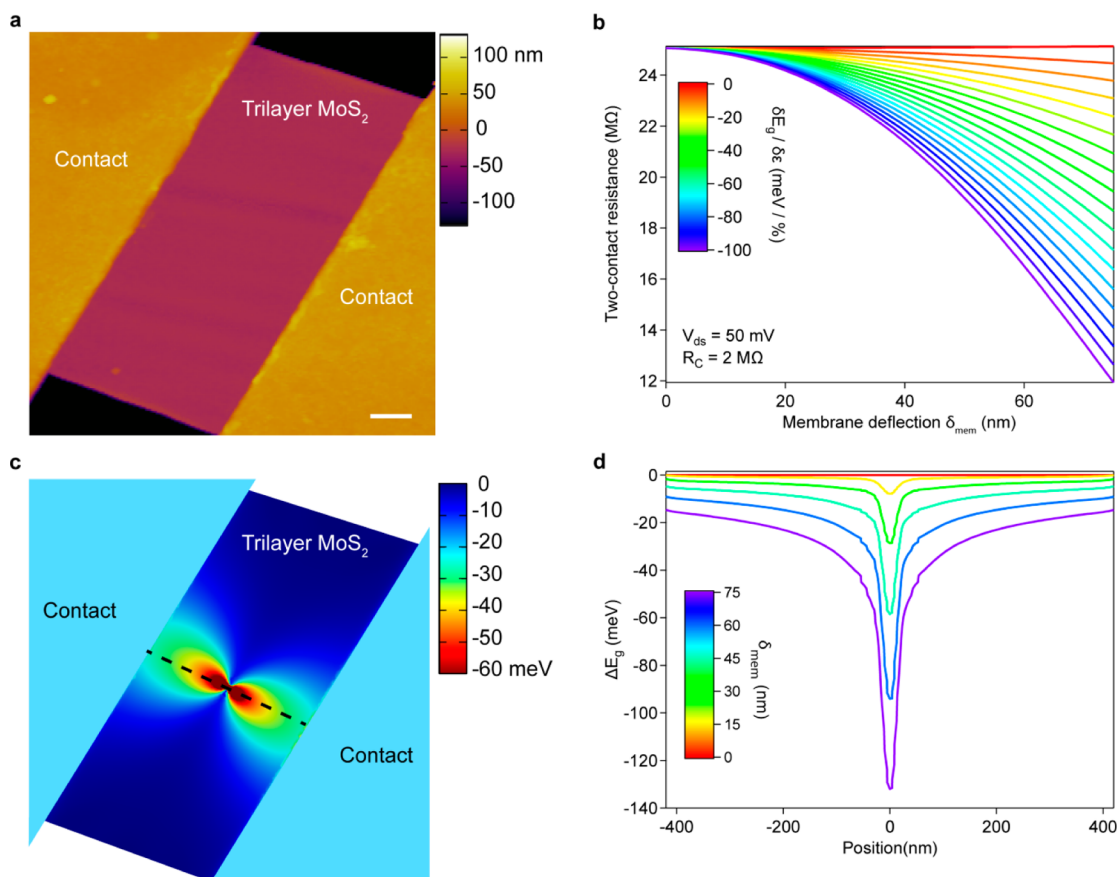


Figure 3. FEM of electromechanical response in a MoS₂ membrane under strain. (a) Topographic AFM image of a trilayer MoS₂ suspended membrane clamped with contact electrodes. The scale bar is 200 nm. (b) FEM simulation of the electromechanical response of the MoS₂ membrane for different values of $\partial E_g/\partial \epsilon$ (c) Simulation result showing the spatial distribution of ΔE_g under deformation $\delta_{\text{mem}} = 75$ nm (d) Profile of bandgap change ΔE_g along the dashed line in c. Areas closer to the tip experience more deformation and, thus, a higher change in the bandgap.

and -22.7 ± 6 meV/% strain for monolayer, bilayer, and trilayer MoS₂, respectively, in excellent agreement with theoretical predictions and optical measurements.^{12,18,23,35}

The bandgap tuning rate is higher in bilayer than in monolayer devices. This result is consistent with previous theoretical and experimental reports.^{12,18,36} The orbital contributions of the band-edge states and their hybridizations are different between the monolayer and bilayer MoS₂ and are differently affected by strain, thus leading to different rates of band gap change. Under tensile strain in the planar direction, the in-plane orbital hybridizations are modified. Due to the Poisson effect, the distance between atomic layers is reduced, which will influence the out-of-plane orbital hybridizations as well. Monolayer MoS₂ consists of only one Mo plane; therefore the Mo d_z² orbitals, which are along the out-of-plane direction, are not affected by strain. On the other hand, in bilayer MoS₂ with two Mo planes, the Poisson contraction leads to a stronger interaction between Mo d_z² orbitals of the two Mo planes. Because of the higher sensitivity of the out-of-plane orbitals to the strain, the indirect band gap of bilayer MoS₂ shows a higher $|\partial E_g/\partial \epsilon|$.¹⁹ More in-depth theoretical investigations are required to explain the effect of strain on orbital interactions, which change the bandgap of trilayer MoS₂.

Using finite element modeling, we can also extract the piezoresistive gauge factor (GF), defined as $GF = (\Delta R/R_0)/\epsilon$ where R_0 is the total resistance of the unstrained MoS₂ channel and ΔR the resistance change under strain ϵ . Although the strain distribution in our membranes is not uniform, it varies

continuously and smoothly, and the strain experienced by an infinitesimally small element in the model is uniform. According to eq 2, the resistance r of a finite element under strain ϵ can be written as $r = r_0 \exp(\alpha \epsilon)$ where r_0 is the resistance in the absence of strain and $\alpha = [1/(2k_B T)] \times [\partial E_g/\partial \epsilon]$. For small strains, we have that the gauge factor $GF \approx \alpha$ (Supporting Information Section 8). Using the values of $\partial E_g/\partial \epsilon$ found for MoS₂, we find that the piezoresistance gauge factor for monolayer, bilayer, and trilayer MoS₂ is -148 ± 19 , -224 ± 19 , and -43.5 ± 11 , respectively, with the negative sign indicating decreasing resistivity with increasing strain. This is in contrast to graphene, where the application of strain results in decreasing Fermi velocity and reduced mobility, resulting in increasing resistivity.³⁷ Moreover, it is interesting to note that the piezoresistive gauge factor is highest in bilayer MoS₂, which is due to the higher sensitivity of the bandgap to strain. The gauge factors of monolayer and bilayer MoS₂ measured in our experiment are 2 orders of magnitude higher than in graphene strain sensors (~ 2)^{37,38} and are comparable to state-of-the-art silicon strain sensors (~ 200).³⁹ Silicon, however, has a much lower fracture strain (0.7%)⁴⁰ than MoS₂ (as high as 11%),¹⁰ implying that the latter would be more suitable for strain measurements on curved surfaces and highly deformable objects such as biological tissue. The large piezoresistive coefficient together with the atomic scale thickness also makes MoS₂ suitable for fabrication of self-sensing nanoelectromechanical systems and transparent strain gauges. Chemical doping⁴¹ could be used in future to reduce the power dissipation in practical devices due to the relatively high device

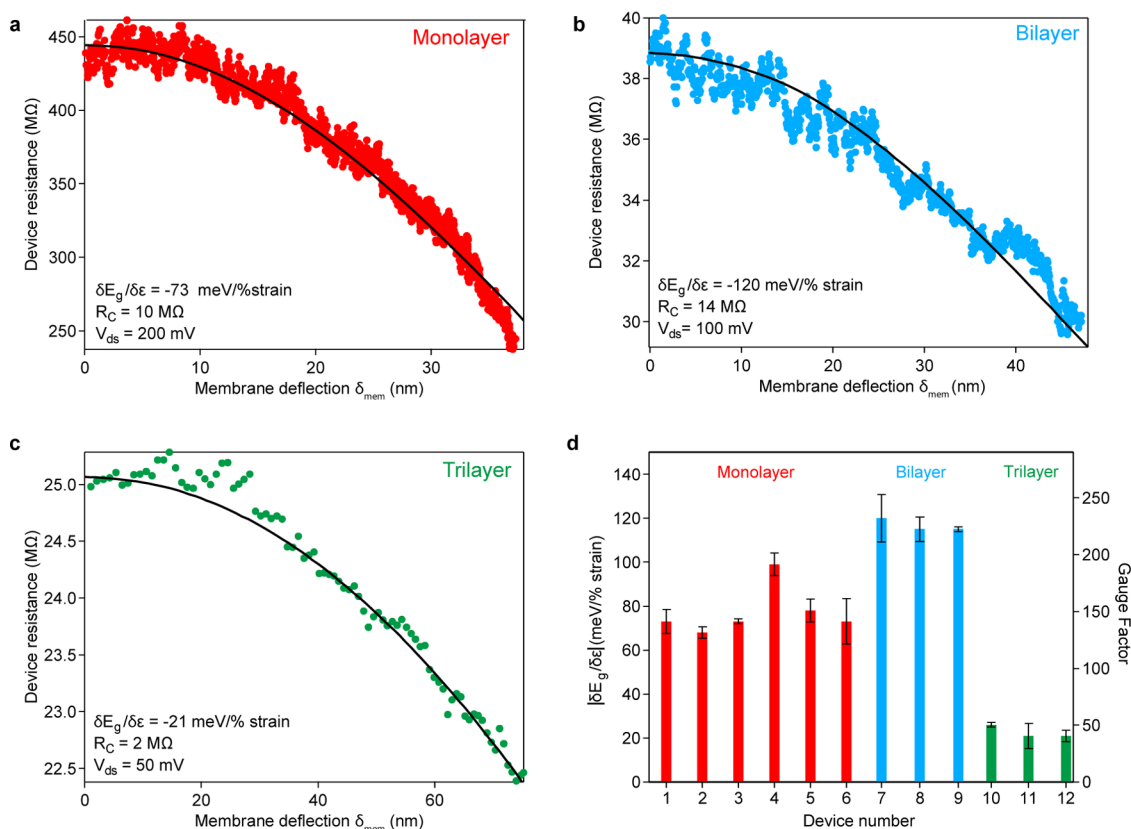


Figure 4. Strain-induced band gap tuning in mono and few-layer MoS₂ and modulation of the device resistance due to mechanical deformation of the MoS₂ membrane. (a) Measurements and the corresponding simulation results for a monolayer MoS₂ indicating a reduction of the band gap $\partial E_g/\partial \epsilon$ with a rate of -73 meV/%. (b) Bilayer MoS₂ with $|\partial E_g/\partial \epsilon| = -120$ meV/% and (c) trilayer MoS₂ with $|\partial E_g/\partial \epsilon| = -21$ meV/%. (d) Extracted rate of band gap change $|\partial E_g/\partial \epsilon|$ and piezoresistive gauge factor for six monolayers, three bilayers, and three trilayers (for the data on geometry of each device see Supporting Information Section 3).

resistance, currently in the megaohm range because of the absence of gating.

In conclusion, we have demonstrated strain-induced tuning of the bandgap and electrical resistance of atomically thin layers of MoS₂. A finite element method analysis was developed to model the experimental observations. We show that the bandgap of MoS₂ decreases under mechanical strain and that MoS₂ has a piezoresistive gauge factor comparable to state-of-the-art silicon strain sensors. The developed methodology is generally applicable to other transition metal dichalcogenide semiconductors. Our study reveals that similarly to CMOS devices,⁴² strain—which can be easily controlled through the device fabrication process—is an effective agent to alter electronic transport properties in MoS₂, enabling its efficient implementation as piezoresistive transducer elements for emerging NEMS sensors.

Methods. *Fabrication of Suspended MoS₂ Devices Clamped at Both Ends.* MoS₂ flakes were mechanically exfoliated onto an intrinsic Si substrate with 270 nm of SiO₂. The substrate is imaged using an optical microscope (Olympus BX51M) equipped with a color camera. We have previously established the correlation between the optical contrast and thickness as measured by AFM for a number of dichalcogenide materials, including MoS₂.⁴³ Mono-, bi-, and trilayer MoS₂ flakes were optically detected with thickness confirmed using AFM topography imaging. Contacts are prepared using standard e-beam lithography and e-beam evaporation of Cr/Au (2 nm/60 nm) and lift-off in acetone. The devices were annealed at

200 °C in order to remove resist residue and decrease the contact resistance. The suspension of the channel is achieved by etching away the underlying SiO₂ using buffered hydrofluoric acid (BOE 7:1). In order to prevent the MoS₂ membranes from collapsing due to the surface tension during the drying process, the suspended MoS₂ was released in a critical point drier (CPD). Prior to measurements, the suspended devices were annealed in vacuum (6.7×10^{-6} mbar) at 150 °C for 20 h in order to remove residues and adsorbates from both surfaces of the membrane.

Electromechanical Measurements. Nanomechanical testing is performed using a commercially available AFM (Asylum Research Cypher). We use Mikromasch HQ probes (Model NSC35/AL BS). The photodetector is calibrated by performing nanoindentation on the SiO₂ substrate. The calibration curve is presented in Supporting Information Figure S2. In addition to the calibration, the spring constant of each cantilever was extracted prior to electromechanical measurements using the thermal noise method.⁴⁴ Current measurements are carried out using a Stanford Research System SR570 current amplifier.

Finite Element Modeling. Finite element modeling was performed using COMSOL. Each of the studied samples was individually modeled using its exact geometry measured by AFM (AC mode). The tip was modeled as a spherical object with a radius 25 nm, which corresponds to the shape and radius of the tip as determined by scanning electron microscopy (Supporting Information Section 2). Simulations performed on similar membranes and for tip radius in the range of 10 to 35 nm, lead to equal outcomes (Supporting Information Section 6).

MoS₂ membranes are described by a Young's modulus of $E = 270 \text{ GPa}^{10}$ and Poisson's ratio $\nu = 0.27$.¹⁰

■ ASSOCIATED CONTENT

Supporting Information

Supplementary figures and discussion related to AFM calibration, additional devices, FEM modeling and piezotronic effects. The Supporting Information is available free of charge on the ACS Publications website at DOI: 10.1021/acs.nanolett.5b01689.

■ AUTHOR INFORMATION

Corresponding Author

*E-mail: andras.kis@epfl.ch.

Author Contributions

S.M. performed the device fabrication, measurements, data analysis, and finite element modeling. A.A. and A.G. contributed to finite element modeling. A.K. designed the experiment and initiated and supervised the work. S.M., A.A., and A.K. wrote the manuscript.

Notes

The authors declare no competing financial interest.

■ ACKNOWLEDGMENTS

The authors acknowledge S. Bertolazzi and D. Ovchinnikov (EPFL) for valuable discussions. Device fabrication was carried out in the EPFL Center for Micro/Nanotechnology (CMI). We thank Z. Benes (CMI) for technical support with e-beam lithography. This work was financially supported by funding from the European Union's Seventh Framework Programme FP7/2007-2013 under Grant Agreement No. 318804 (S.N.M.) and was carried out in frames of the Marie Curie ITN network "MoWSeS" (grant no. 317451). We acknowledge funding by the EC under the Graphene Flagship (grant agreement no. 604391).

■ REFERENCES

- (1) Wang, Q. H.; Kalantar-Zadeh, K.; Kis, A.; Coleman, J. N.; Strano, M. S. *Nat. Nanotechnol.* **2012**, *7* (11), 699–712.
- (2) Lebegue, S.; Eriksson, O. *Phys. Rev. B: Condens. Matter Mater. Phys.* **2009**, *79* (11), 115409.
- (3) Li, T.; Galli, G. J. *Phys. Chem. C* **2007**, *111* (44), 16192–16196.
- (4) Splendiani, A.; Sun, L.; Zhang, Y.; Li, T.; Kim, J.; Chim, C.-Y.; Galli, G.; Wang, F. *Nano Lett.* **2010**, *10* (4), 1271–1275.
- (5) Mak, K. F.; Lee, C.; Hone, J.; Shan, J.; Heinz, T. F. *Phys. Rev. Lett.* **2010**, *105* (13), 136805.
- (6) Kuc, A.; Zibouche, N.; Heine, T. *Phys. Rev. B: Condens. Matter Mater. Phys.* **2011**, *83* (24), 245213.
- (7) Radisavljevic, B.; Radenovic, A.; Brivio, J.; Giacometti, V.; Kis, A. *Nat. Nanotechnol.* **2011**, *6* (3), 147–150.
- (8) Lopez-Sanchez, O.; Lembke, D.; Kayci, M.; Radenovic, A.; Kis, A. *Nat. Nanotechnol.* **2013**, *8* (7), 497–501.
- (9) Jiang, J.-W.; Park, H. S.; Rabczuk, T. *Nanoscale* **2014**, *6* (7), 3618.
- (10) Bertolazzi, S.; Brivio, J.; Kis, A. *ACS Nano* **2011**, *5* (12), 9703–9709.
- (11) Kaplan-Ashiri, I.; Cohen, S. R.; Gartsman, K.; Ivanovskaya, V.; Heine, T.; Seifert, G.; Wiesel, I.; Wagner, H. D.; Tenne, R. *Proc. Natl. Acad. Sci. U. S. A.* **2006**, *103* (3), 523–528.
- (12) He, K.; Poole, C.; Mak, K. F.; Shan, J. *Nano Lett.* **2013**, *13* (6), 2931–2936.
- (13) Johari, P.; Shenoy, V. B. *ACS Nano* **2012**, *6* (6), 5449–5456.
- (14) Ghorbani-Asl, M.; Borini, S.; Kuc, A.; Heine, T. *Phys. Rev. B: Condens. Matter Mater. Phys.* **2013**, *87* (23), 235434.
- (15) Shi, H.; Pan, H.; Zhang, Y.-W.; Yakobson, B. I. *Phys. Rev. B: Condens. Matter Mater. Phys.* **2013**, *87* (15), 155304.
- (16) Yun, W. S.; Han, S. W.; Hong, S. C.; Kim, I. G.; Lee, J. D. *Phys. Rev. B: Condens. Matter Mater. Phys.* **2012**, *85* (3), 033305.
- (17) Lu, P.; Wu, X.; Guo, W.; Zeng, X. C. *Phys. Chem. Chem. Phys.* **2012**, *14* (37), 13035–13040.
- (18) Li, T. *Phys. Rev. B: Condens. Matter Mater. Phys.* **2012**, *85* (23), 235407.
- (19) Scalise, E.; Houssa, M.; Pourtois, G.; Afanas'ev, V. V.; Stesmans, A. *Phys. E* **2014**, *56*, 416–421.
- (20) Cheiwchanchamnangij, T.; Lambrecht, W. R. L. *Phys. Rev. B: Condens. Matter Mater. Phys.* **2012**, *85* (20), 205302.
- (21) Wu, W.; Wang, L.; Li, Y.; Zhang, F.; Lin, L.; Niu, S.; Chenet, D.; Zhang, X.; Hao, Y.; Heinz, T. F.; Hone, J.; Wang, Z. L. *Nature* **2014**, *514* (7523), 470–474.
- (22) Zhu, H.; Wang, Y.; Xiao, J.; Liu, M.; Xiong, S.; Wong, Z. J.; Ye, Z.; Ye, Y.; Yin, X.; Zhang, X. *Nat. Nanotechnol.* **2015**, *10*, 151–155.
- (23) Castellanos-Gomez, A.; Roldán, R.; Cappelluti, E.; Buscema, M.; Guinea, F.; van der Zant, H. S. J.; Steele, G. A. *Nano Lett.* **2013**, *13* (11), 5361–5366.
- (24) Conley, H. J.; Wang, B.; Ziegler, J. I.; Haglund, R. F., Jr.; Pantelides, S. T.; Bolotin, K. I. *Nano Lett.* **2013**, *13* (8), 3626–3630.
- (25) Li, M.; Tang, H. X.; Roukes, M. L. *Nat. Nanotechnol.* **2007**, *2* (2), 114–120.
- (26) Tombler, T. W.; Zhou, C.; Alexseyev, L.; Kong, J.; Dai, H.; Liu, L.; Jayanthi, C. S.; Tang, M.; Wu, S.-Y. *Nature* **2000**, *405* (6788), 769–772.
- (27) Mott, N. F. *J. Phys. Colloq.* **1976**, *37* (C4), C4–C301–C4–C306.
- (28) Hui, Y. Y.; Liu, X.; Jie, W.; Chan, N. Y.; Hao, J.; Hsu, Y.-T.; Li, L.-J.; Guo, W.; Lau, S. P. *ACS Nano* **2013**, *7* (8), 7126–7131.
- (29) Harada, N.; Sato, S.; Yokoyama, N. *J. Appl. Phys.* **2014**, *115* (3), 034505.
- (30) Bhattacharyya, S.; Pandey, T.; Singh, A. K. *Nanotechnology* **2014**, *25* (46), 465701.
- (31) Koskinen, P.; Fampiou, I.; Ramasubramaniam, A. *Phys. Rev. Lett.* **2014**, *112* (18), 186802.
- (32) Yue, Q.; Kang, J.; Shao, Z.; Zhang, X.; Chang, S.; Wang, G.; Qin, S.; Li, J. *Phys. Lett. A* **2012**, *376* (12–13), 1166–1170.
- (33) Dong, L.; Namburu, R. R.; O'Regan, T. P.; Dubey, M.; Dongare, A. M. *J. Mater. Sci.* **2014**, *49* (19), 6762–6771.
- (34) Li, S.-L.; Komatsu, K.; Nakaharai, S.; Lin, Y.-F.; Yamamoto, M.; Duan, X.; Tsukagoshi, K. *ACS Nano* **2014**, *8* (12), 12836–12842.
- (35) Feng, J.; Qian, X.; Huang, C.-W.; Li, J. *Nat. Photonics* **2012**, *6* (12), 866–872.
- (36) Zhu, C. R.; Wang, G.; Liu, B. L.; Marie, X.; Qiao, X. F.; Zhang, X.; Wu, X. X.; Fan, H.; Tan, P. H.; Amand, T.; Urbaszek, B. *Phys. Rev. B: Condens. Matter Mater. Phys.* **2013**, *88* (12), 121301.
- (37) Smith, A. D.; Niklaus, F.; Pausa, A.; Vaziri, S.; Fischer, A. C.; Sterner, M.; Forsberg, F.; Delin, A.; Esseni, D.; Palestri, P.; Östling, M.; Lemme, M. C. *Nano Lett.* **2013**, *13*, 3237.
- (38) Huang, M.; Pascal, T. A.; Kim, H.; Goddard, W. A.; Greer, J. R. *Nano Lett.* **2011**, *11* (3), 1241–1246.
- (39) Kanda, Y. *Sens. Actuators, A* **1991**, *28* (2), 83–91.
- (40) Petersen, K. E. *Proc. IEEE* **1982**, *70* (5), 420–457.
- (41) Kiriya, D.; Tosun, M.; Zhao, P.; Kang, J. S.; Javey, A. *J. Am. Chem. Soc.* **2014**, *136* (22), 7853–7856.
- (42) Chidambaram, P. R.; Bowen, C.; Chakravarthi, S.; Machala, C.; Wise, R. *IEEE Trans. Electron Devices* **2006**, *53* (5), 944–964.
- (43) Benameur, M. M.; Radisavljevic, B.; Heron, J. S.; Sahoo, S.; Berger, H.; Kis, A. *Nanotechnology* **2011**, *22* (12), 125706.
- (44) Hutter, J. L.; Bechhoefer, J. *Rev. Sci. Instrum.* **1993**, *64* (7), 1868–1873.
- (45) Feldman, J. L. *J. Phys. Chem. Solids* **1976**, *37* (12), 1141–1144.

Supplementary Information

for

Piezoresistivity and Strain-induced Band Gap Tuning in Atomically Thin MoS₂

Sajedeh Manzeli, Adrien Allain, Amirhossein Ghadimi, Andras Kis*

Electrical Engineering Institute, École Polytechnique Fédérale de Lausanne (EPFL), CH-1015 Lausanne, Switzerland

**Correspondence should be addressed to: Andras Kis, andras.kis@epfl.ch*

1. Nanoindentation experiment and calibration of the photodetector sensitivity

In our experiment, the MoS₂ membrane is first imaged and located using the AFM in the noncontact amplitude modulation mode. Once the membrane is imaged, the non-conductive AFM tip is positioned on top of the center of the membrane. To perform a nanoindentation measurement in the contact mode, a piezo scanner moves the stage towards the cantilever with a controlled speed. In step (1) illustrated in figure S1, the tip is far away from the surface and there is no interaction between the tip and the membrane, therefore the cantilever's deflection is constant. Step (2) in figure S1, indicates the critical distance for which the tip experiences an attractive force and snaps to the surface and thus the cantilever's deflection drops abruptly to a negative value ($z_{\text{piezo}} = 0$). By further extension of the piezo scanner, the tip deforms the membrane while bending up due to the reaction force. Hence, the increasing deflection of the cantilever towards positive values (step (3) in figure S1). The extension cycle continues until the deflection of the cantilever reaches a predefined setpoint which defines the maximum deformation of the membrane. Once the setpoint is reached, the retraction cycle starts. The scanner moves downward, releasing the strain on the membrane which is translated in a reduced cantilever's deflection (steps (4) to (6) in figure S1). The drain current and the cantilever deflection are acquired as a function of scanner position (z_{piezo}) during both cycles of extension and retraction. The kink in the retraction curve step (5) is due to the adhesion between tip and MoS₂ upon detaching. This type of adhesion has also been observed in suspended graphene membranes or carbon nanotubes^{1,2}.

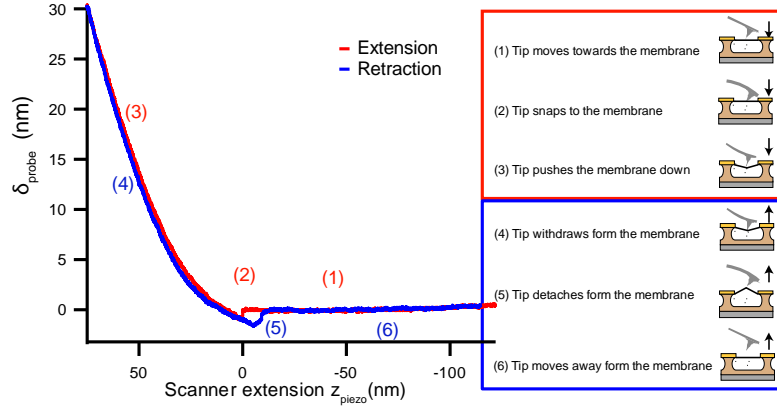


Figure S1. Nanoindentation experiment. Different steps in a typical nanoindentation experiment with extension (red) and retraction curves (blue).

The cantilever deflection is detected by means of a position-sensitive photodetector (PSD) and is reported in volts, resulting in δ_{volts} . In order to assess the value of cantilever's deflection in nm, the PSD needs to be calibrated. This is achieved by deforming the cantilever on the hard SiO_2 substrate, this way the deformation of the substrate is negligible compared to the deflection of the cantilever. In this case there is a one-to-one correspondence between the deflection of the cantilever and the voltage measured by the PSD. The inverse optical lever sensitivity InvOLS is then defined as³:

$$\text{InvOLS} = \frac{d(z_{\text{piezo}})}{d(\delta_{\text{volts}})} \quad (\text{S1})$$

where δ_{volts} is the change in the voltage signal on the PSD due to the deflection of cantilever. Figure S2 shows a typical calibration curve where $\text{InvOLS} = 0.5 \text{ nm/V}$ is extracted from inverse of the slope of the linear fit (black curve).

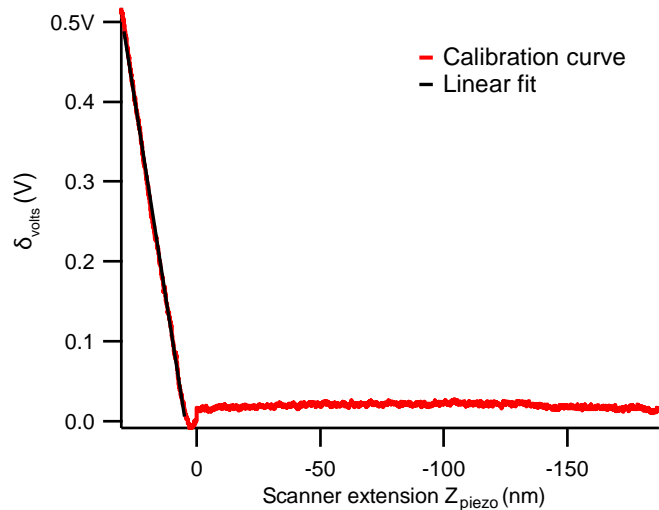


Figure S2. Calibration of the photodetector. The calibration curve acquired by deforming the cantilever on the hard substrate (red curve). The inverse of the slope of linear fit (black curve) to the data results in the inverse optical lever sensitivity of 0.5 nm/V .

Freestanding membranes were imaged using AC mode (Figure S3a). The cross section of the AFM image along the red line in Figure S3a shows the step-height at the edge of the

membrane and that MoS₂ is suspended ~200nm above the substrate. The flat image indicates effective clamping and the absence of defects. The use of freestanding MoS₂ allows elimination of substrate effects such as doping due to trapped charges in the oxide and at the interface.

During the nanoindentation experiment, the piezo scanner is moved in the vertical direction with a speed of 40nm/s to ensure that the loading and unloading of the membrane is performed in a quasi-static manner. The AFM setup is equipped with an air temperature controller (ATC) to keep the temperature in the chamber constant (30 °C) and minimize the mechanical drift. The imaging was repeated every 300 seconds to monitor the tip position on the membrane and verify that the drift was negligible. Repetition of imaging also allowed monitoring the degradation of the tip which will show its effect in the sharpness of the edges.

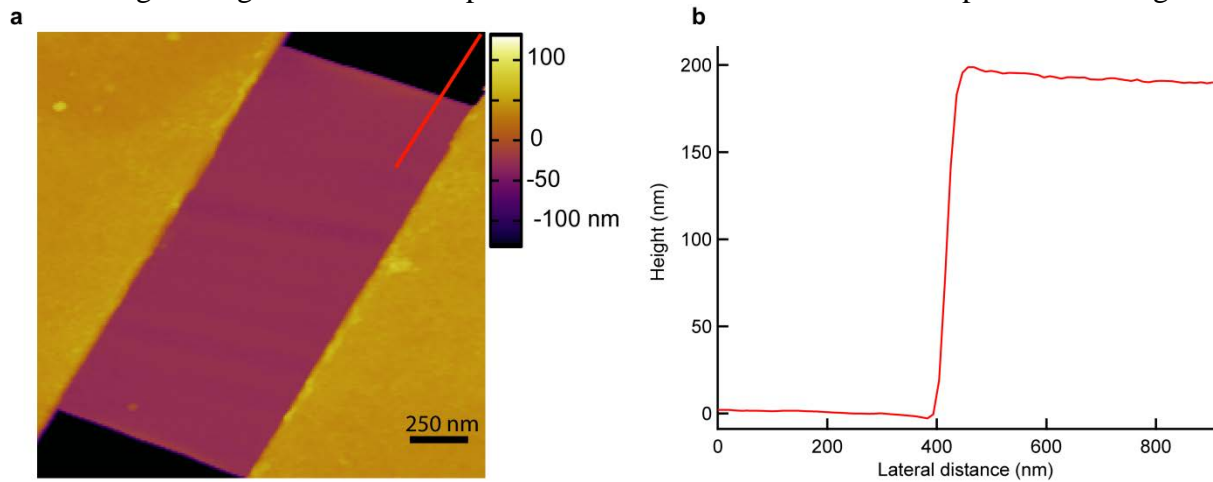


Figure S3. Topographic AFM image of suspended MoS₂ membrane **a**, Atomic force microscope image of a suspended MoS₂ membrane **b**, Cross-sectional plot along the red line in **a**.

2. AFM tip geometry

Mikromasch HQ probes (Model NSC35/AL BS) were used. In order to measure the tip radius, scanning electron microscopy (SEM) was used. Figure S4a and b show the SEM image of a tip from the side to measure the radius and Figure S4c and d show it from the top to confirm the hemispheric shape of the tip.

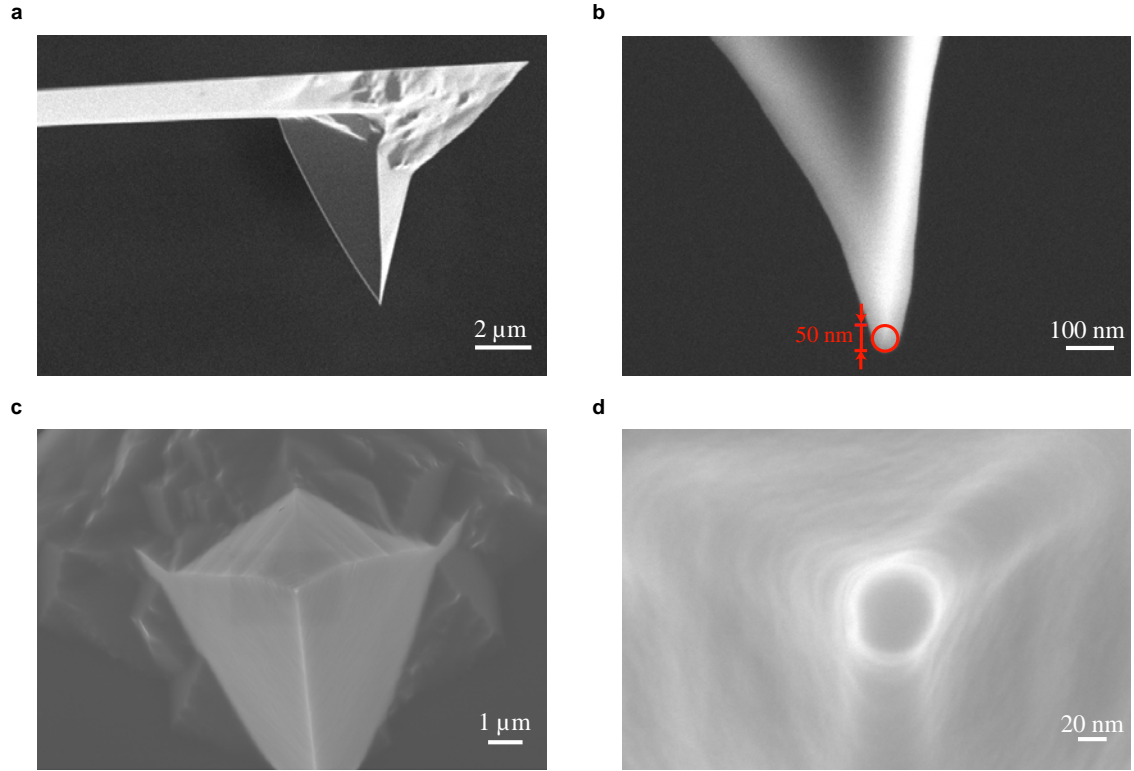


Figure S4. Measurement of AFM tip geometry using scanning electron microscopy. **a**, Side view SEM image of the AFM probe. **b**, Magnified side view SEM image of the AFM probe. The diameter of the tip is is ~50nm. **c**, top view SEM image of the AFM tip. **d**, Magnified SEM image of the AFM tip confirms the hemispherical shape of the tip.

3. Bandgap change rate extracted for monolayer, bilayer and trilayer MoS₂ membranes with different geometries

Device number	Width [nm]	Length[nm]	Channel thickness	$\partial E_g / \partial \epsilon$ [meV/%]
1	990	570	1L	-73 ± 6
2	1270	804	1L	-68 ± 3
3	85	930	1L	-73 ± 1
4	105	1400	1L	-99 ± 5
5	1300	1000	1L	-78 ± 5
6	6000	1000	1L	-73 ± 10
7	700	1300	2L	-120 ± 10
8	200	700	2L	-115 ± 6
9	3650	1000	2L	-115 ± 1
10	2800	850	3L	-26 ± 1
11	2700	950	3L	-21 ± 6
12	80	780	3L	-21 ± 3

Table S1. The strain induced bandgap change rate for mono-, bi- and trilayer MoS₂ membranes

The error bars are calculated from the uncertainties in the measurement of input parameters propagating in the calculated results. We find that the dominant source of error is the uncertainty in the measurement of the membrane geometry from the AFM topography image which may be due to the artifacts such as tip convolution effect.

4. Mechanical failure of membranes

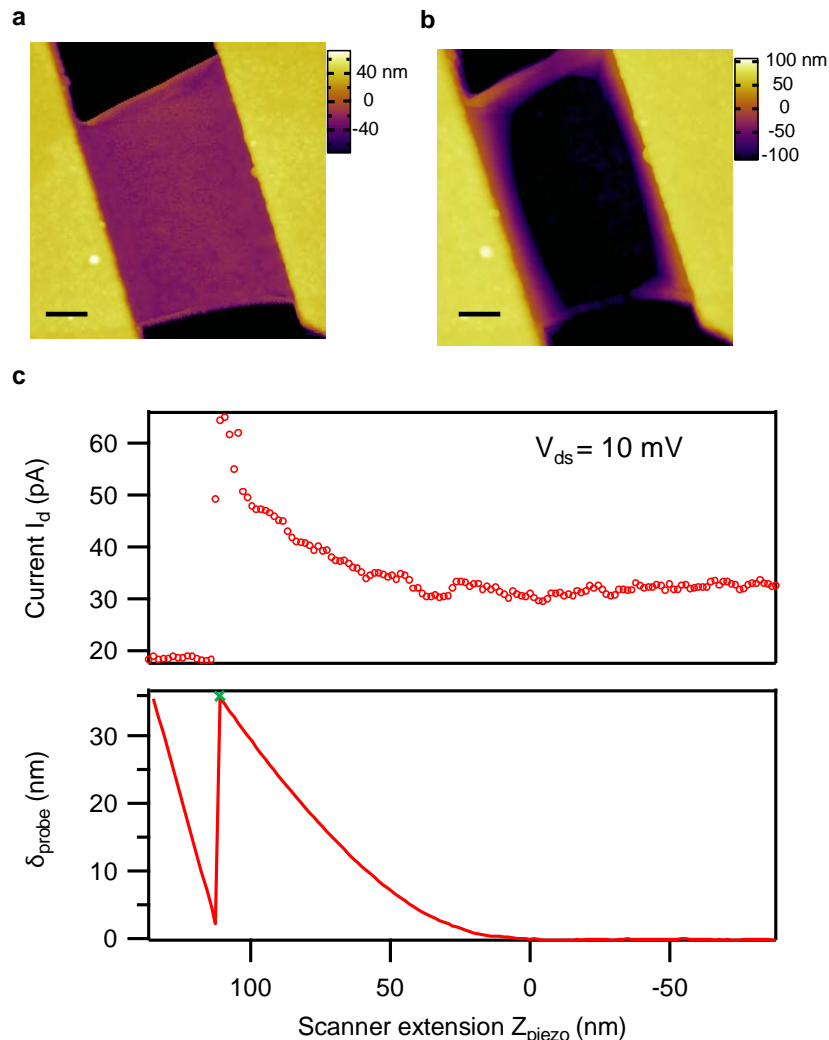


Figure S5. Mechanical failure of suspended devices. **a**, AFM image of the suspended single layer membrane before electromechanical measurements. **b**, AFM image of the collapsed membrane after measurements. Scale bar is 200nm. **c**, The nanoindentation curve shows the modulation of current due to deformation of membrane up to mechanical failure point which is marked by green cross. At the collapse of membrane, both the current I_d and the probe deflection δ_{probe} drop sharply. Further extension of the piezo scanner results in probe deflection on top of the substrate while the current remains constant.

In order to measure the electromechanical response of each membrane, it is deformed in several nanoindentation cycles with the deformation increasing in each cycle. For each membrane the deformation is systematically increased up to the mechanical failure point. The maximum strain achieved in membranes is calculated to be 7%. Figure S5a. and S5b, show a single layer membrane before measurements and after mechanical failure, which in this case has most probably occurred due to van der Waals interaction between the substrate and the membrane. The corresponding nanoindentation curve is illustrated in Figure S5c. The current increases as soon as the membrane undergoes deformation and the same trend continues up to the mechanical failure point (green cross in Figure S5c) at which both the current I_d and the probe deflection δ_{probe} drop sharply. By further extension of piezo scanner, the probe starts

being deflected however this time on top of the hard substrate and the current remains constant.

5. Extracting conductivity as a function of strain

In the sub-threshold regime and at room temperature, the conductivity is expressed as⁴:

$$\sigma = \sigma_0 \exp \left[-\frac{E_C - E_F}{k_B T} \right] \quad (S2)$$

where σ_0 is the minimum conductivity defined by the hopping distance, E_C is the conduction band edge, E_F is the Fermi energy, k_B is the Boltzmann constant and T the temperature. The conductivity in the relaxed (σ_{rel}) and deformed state (σ_{def}), is written respectively as:

$$\sigma_{rel} = \sigma_0 \exp \left[-\frac{E_{C,rel} - E_F}{k_B T} \right] \quad (S3)$$

$$\sigma_{def} = \sigma_0 \exp \left[-\frac{E_{C,def} - E_F}{k_B T} \right] \quad (S4)$$

Therefore:

$$\sigma_{def} = \sigma_{rel} \exp \left[-\frac{E_{C,def} - E_{C,rel}}{k_B T} \right] = \sigma_{rel} \exp \left[-\frac{\Delta E_C}{k_B T} \right] \quad (S5)$$

Assuming a symmetric reduction of bandgap under strain⁵, ΔE_C would be equal to $\Delta E_g/2$. Hence:

$$\sigma_{def} = \sigma_{rel} \exp \left[-\frac{\Delta E_g}{2k_B T} \right] \quad (S6)$$

for small strains (up to 7% in our case), the bandgap is expected to change linearly with strain^{6,7}. This means that $\Delta E_g = (\partial E_g / \partial \epsilon) \times \epsilon$ where ϵ is strain and $\partial E_g / \partial \epsilon$ is the rate of bandgap change with strain. Therefore:

$$\sigma_{def} = \sigma_{rel} \exp \left[-\frac{\epsilon}{2k_B T} \frac{\partial E_g}{\partial \epsilon} \right] \quad (S7)$$

Eq. (S7) states that, for bandgap which shrinks under strain, the conductivity increases.

6. Finite element modeling

Finite element models are built using COMSOL 5 to reveal the effect of deformation on the bandgap of MoS₂ membranes. We simulated the spatial distribution of strain induced by the tip in the semiconducting channel and thus we can obtain the modulation of bandgap induced by the strain. Each sample is modeled using its exact geometry measured by AFM in AC mode. The tip was modelled as a spherical object with a radius of 25 nm which corresponds to the shape and radius of the tip as determined by scanning electron microscopy (Figure

S4d). The spherical shape of the tip avoids stress singularity at the center and the elastic strain does not diverge near the center of the membrane. The boundary conditions are set in a way that the membrane is clamped from the two edges and is indented by the sphere in the z direction by a predefined value of δ_{mem} . To analyse the electrical response, a DC bias voltage is applied between the clamped edges of the membrane and the conductivity of the membrane at each point depends on strain according to the Eq. S7. The membrane and the tip are meshed using “free triangular” and “free tetrahedral” elements respectively and the model is solved using a stationary solver. In order to get a complete picture, it is necessary to take into account that the suspended devices involve the MoS_2 channel (piezoresistive material) and the electrical contacts with a certain contact resistance. Ignoring the effect of contact resistance will result in an over-estimate for the bandgap change rate $\partial E_g/\partial \epsilon$, while in another extreme if the value of the contact resistance is the dominant part of the total device resistance, the effect of strain on the suspended channel is masked by the larger in-series contact resistance. In order to consider the effect of contact resistance, it is added as a fitting parameter to our model. Consequently, the fitting parameters of our FEM analysis were the band gap change rate $\partial E_g/\partial \epsilon$ and the contact resistance R_C . For each value of δ_{mem} , the total conductance and thus the total resistance of the deflected membrane is calculated from the strain distribution. Each of the measured membranes was simulated by conducting three dimensional parametric sweeps of δ_{mem} , $\partial E_g/\partial \epsilon$ and R_C and subsequently calculating the total resistance in each step. Corresponding to the device presented in Figure 3 of the main text, representative output curves of total resistance vs. membrane deflection for $\partial E_g/\partial \epsilon = -21 \text{ meV}/\%$ strain and contact resistance in the range of 0 and $24 \text{ M}\Omega$ is given in Figure S6a. For contact resistance $R_C = 0$, the electromechanical response shows the highest sensitivity to the deflection of the membrane δ_{mem} . On the other hand for $R_C = 24 \text{ M}\Omega$, the sensitivity of response to applied deformation is very small, due to the fact that the large contact resistance masks the piezoresistive behaviour.

Furthermore, considering the radius variation between different tips which can occur during their fabrication, a set of tests have been performed on the sensitivity of the simulation result on the tip radius. For the tip radius variations in the range of 10 nm to 35 nm, which is the range of variation in the radius as provided by the manufacturer, a set of simulations has been carried out. The results of these simulations on the membrane of Figure 3 (main text) and on one of the measured ribbons are presented in Figure S6b and S6c respectively. As shown in Figures S6b and S6c, for both the device N°11 in the shape of a membrane or device N°4 in the shape of a ribbon, the results are perfectly matching for tip radii of 10 nm, 25 nm and 35 nm. This confirms that the simulation results are insensitive to small variations of the tip radius.

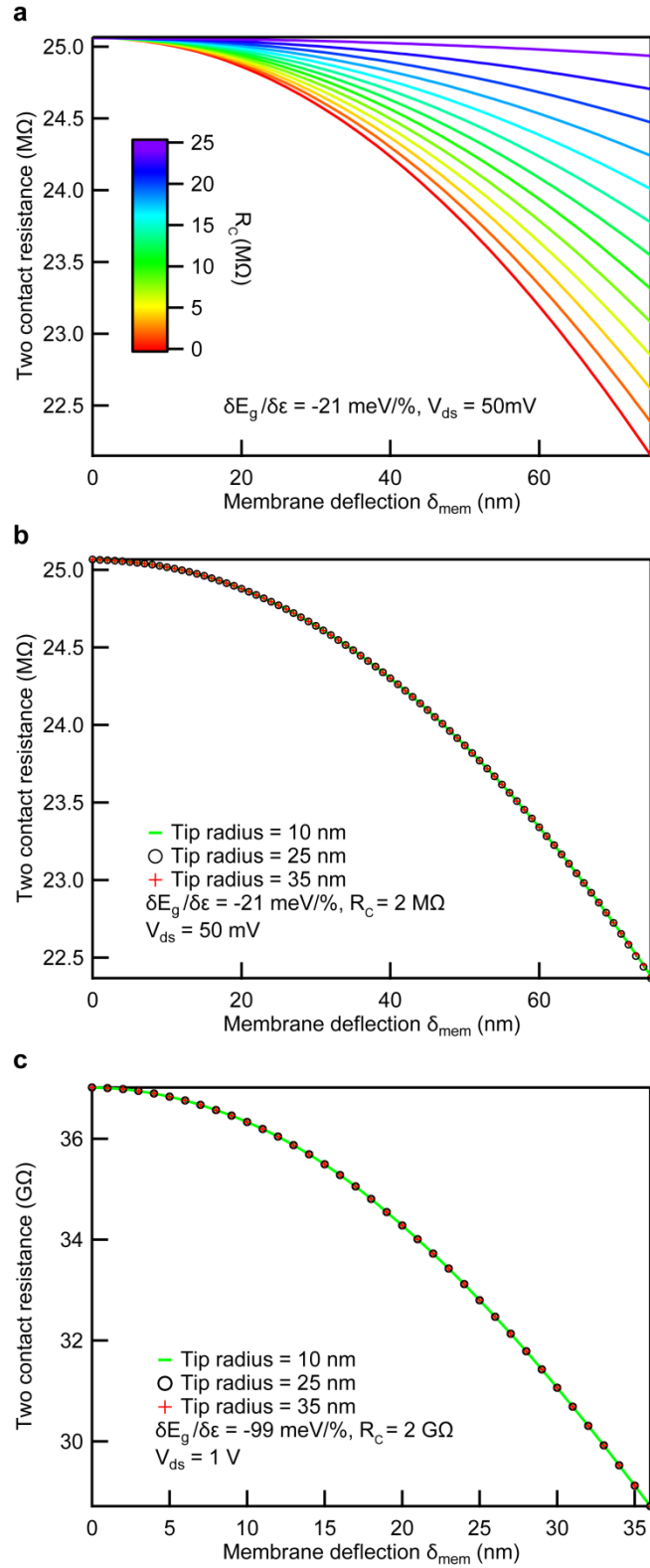


Figure S6. FEM modeling of the effect of contact resistance and variations in tip radius. **a**, Effect of contact resistance on the electromechanical behavior. In the absence of any contact resistance in series with the piezoresistive channel, the device shows the highest sensitivity to the applied deformation. The sensitivity of response to membrane deformation decreases with increasing contact resistance. **b**, The piezoresistive behaviour of a membrane under deformation, simulated with the tips of different radii give the same result. **c**, The piezoresistive behaviour of a ribbon under deformation, simulated with the tips of different radii gives the same results.

7. Reproducibility of the piezoresistive response

Each membrane is measured in several cycles of nanoindentation experiment with the membrane deflection δ_{mem} increasing every time. Figure S7 shows the measured piezoresistive behavior of the monolayer device from Figure 4a of the main text (device N°1), for different values of δ_{mem} . As shown in Figure S7, the resistance of the membrane acquired during several successive cycles of deformation follows the same curve.

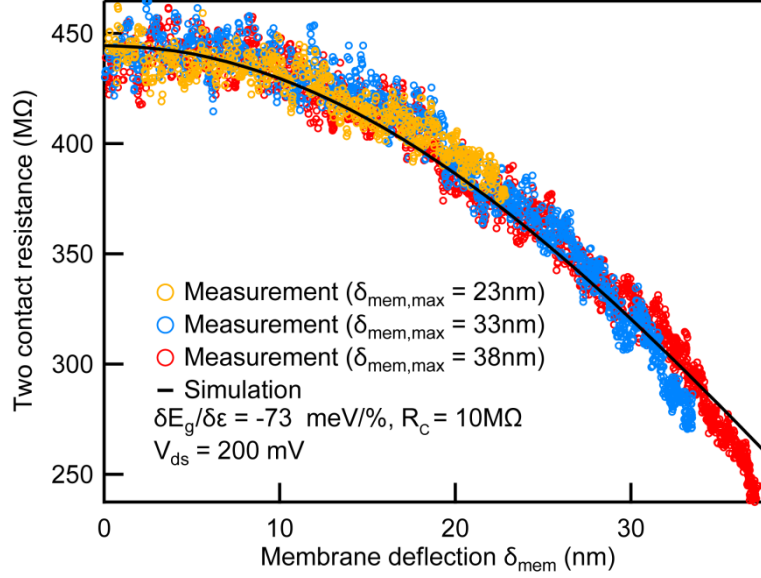


Figure S7. Reproducibility of the piezoresistive response. The electromechanical response of device N°1. When deformed in three cycles each time to different values, the response is reproducible.

8. Extracting the gauge factor for MoS₂ membranes

The piezoresistive gauge factor (GF) is defined as $GF = (\Delta R/R_0)/\epsilon$ where R_0 is the total resistance of the unstrained MoS₂ channel and ΔR its change under strain ϵ . Although the strain distribution in our membranes is not uniform, it varies continuously and smoothly and the strain experienced by an infinitesimally small element in the model is uniform. According to Eq. (S7), the resistance r of a finite element under strain ϵ can be written as $r = r_0 \exp(\alpha\epsilon)$ where r_0 is the resistance in the absence of strain and $\alpha = [1/(2k_B T)] \times [\partial E_g / \partial \epsilon]$. The elemental gauge factor gf is then calculated as:

$$gf = \frac{\delta r / r_0}{\epsilon} = \frac{1}{\epsilon} \frac{r_0 [\exp(\alpha\epsilon) - 1]}{r_0} \quad (\text{S8})$$

For levels of strain used in this work (smaller than 7%), the above expression could be written as:

$$gf = \frac{1}{\epsilon} \frac{r_0 [1 + \alpha\epsilon - 1]}{r_0} = \alpha \quad (\text{S9})$$

Since $\alpha = [1/(2k_B T)] \times [\partial E_g / \partial \epsilon]$ has the same value for all finite elements on the membrane, the elemental gauge factor gf for all finite elements is equal. The total resistance of the membrane is composed of the resistance of these small elements connected in series and in parallel. In order to assess the gauge factor of the membrane, we need to know the gauge factor for the elements connected in series and in parallel. In Figure S8 the elements (a) and

(b) are connected in series and the elements (a) and (c) are connected in parallel, each with an elemental gauge factor α :

$$r_{series} = r_a + r_b = r_{a,0}(1 + \alpha\varepsilon) + r_{b,0}(1 + \alpha\varepsilon) = (r_{a,0} + r_{b,0})(1 + \alpha\varepsilon) = r_{series,0}(1 + \alpha\varepsilon) \quad (S10)$$

therefore:

$$gf_{series} = \frac{1}{\varepsilon} \frac{r_{series} - r_{series,0}}{r_{series,0}} = \alpha \quad (S11)$$

For the case of parallel elements:

$$r_{parallel} = \frac{r_a r_c}{r_a + r_c} = \frac{r_{a,0} r_{c,0} (1 + \alpha\varepsilon)^2}{(r_{a,0} + r_{c,0})(1 + \alpha\varepsilon)} = r_{parallel,0}(1 + \alpha\varepsilon) \quad (S12)$$

$$gf_{parallel} = \frac{1}{\varepsilon} \left(\frac{r_{parallel} - r_{parallel,0}}{r_{parallel,0}} \right) = \alpha \quad (S13)$$

These calculations show that piezoresistances of equal gauge factor when in series or in parallel lead to a total resistance of the same gauge factor. As a result the gauge factor for MoS₂ membrane GF is equal to α .

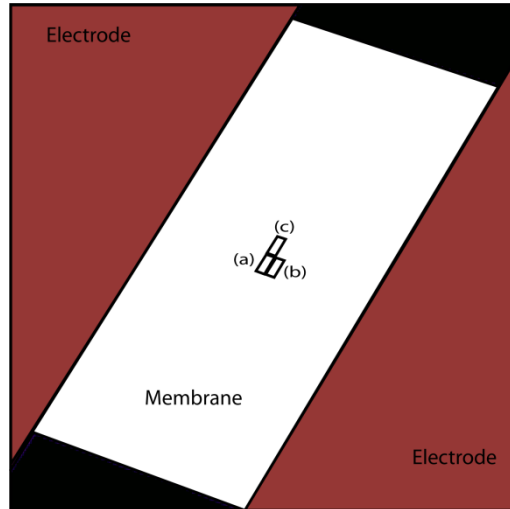


Figure S8. Piezoresistive gauge factor of MoS₂. The membrane consists of infinitesimally small elements connected in series and in parallel each with a piezoresistive gauge factor α . The gauge factor of piezoresistive membrane GF is calculated to be equal to α .

9. Piezotronic effect in MoS₂

In addition to piezoresistivity, MoS₂ flakes with odd number of layers are predicted to be piezoelectric as a result of broken inversion symmetry. In MoS₂ flakes with even numbers of layers, piezoelectricity disappears due to the preservation of inversion symmetry^{8,9}. Therefore, while the response of the bilayer devices to strain is purely piezoresistive, the modulation of charge transport in monolayer and trilayer devices, in addition to piezoresistive behaviour, might also be influenced by the piezotronic effect. In piezotronic effect, the strain induced polarization charges may appear at the zigzag edges of MoS₂ and modulate the transport current.

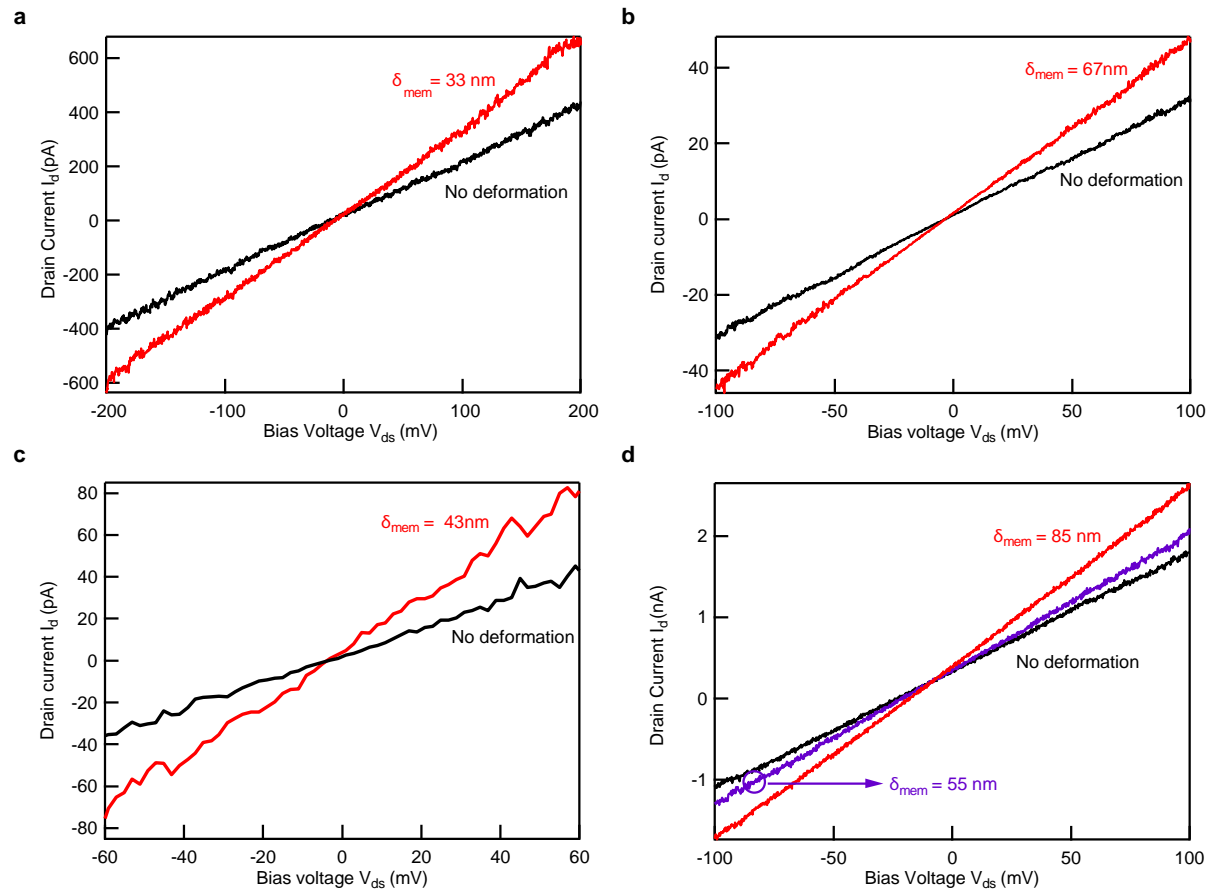


Figure S9. The direct current transport behavior of single layer membranes under deformation. From table S1: **a**, Device N°1. **b**, Device N°2. **c**, Device N°3. **d**, Device N°6. For opposite polarities of bias voltage, the symmetric increase of current under application of strain is the sign of piezoresistive response rather than the piezotronic effect.

The modulation of carrier transport by strain would be asymmetric under opposite drain bias for a piezotronic effect and would be symmetric for a piezoresistive effect⁸. Figure S9 demonstrates the output electrical characterization of four monolayer MoS₂ devices (devices 1, 2, 3 and 6 from table S1) with the symmetrical effect of strain under opposite polarities of bias voltage which is a sign of piezoresistive behaviour. Overall, we have not observed a sign of piezotronic effect in our monolayer and trilayer devices. This can be explained by an important difference between piezoresistive effect and piezoelectric effect. Piezoresistive effect is nearly independent of crystallographic orientation due to the fact that MoS₂ monolayer has isotropic in-plane elasticity owing to its hexagonal space group symmetry^{6,7,10}. On the other hand, piezoelectric effects in MoS₂ depend on the crystallographic orientation where strain induced polarization vector would be along the ‘armchair’ direction^{8,9}. Therefore

a strong piezoelectric signal is observed only for the devices with contact–MoS₂ interface parallel to ‘zigzag’ direction. In our devices the source and drain electrodes are made at an arbitrary angle, which means that the chances of having the zigzag edge at the contact interface and thus the probability of reading out a strong piezo electric signal is very low. On the other hand, due to the intrinsic and environmental doping, free charge carriers are present in MoS₂. These charge carriers may partially screen the piezoelectric polarization charges and hence reduce the piezoelectric effect⁸. A minor piezotronic effect could still be present, which might be one of the factors responsible for device-to-device variations of the bandgap change rate $\partial E_g/\partial \epsilon$.

REFERENCES

- (1) Huang, M.; Pascal, T. A.; Kim, H.; Goddard, W. A.; Greer, J. R. *Nano Lett.* **2011**, *11* (3), 1241–1246.
- (2) Minot, E. D.; Yaish, Y.; Sazonova, V.; Park, J.-Y.; Brink, M.; McEuen, P. L. *Phys. Rev. Lett.* **2003**, *90* (15), 156401.
- (3) Hu, Z.; Seeley, T.; Kossek, S.; Thundat, T. *Rev. Sci. Instrum.* **2004**, *75* (2), 400–404.
- (4) Mott, N. F. *J. Phys. Colloq.* **1976**, *37* (C4), C4–C301 – C4–C306.
- (5) Castellanos-Gomez, A.; Roldán, R.; Cappelluti, E.; Buscema, M.; Guinea, F.; van der Zant, H. S. J.; Steele, G. A. *Nano Lett.* **2013**, *13* (11), 5361–5366.
- (6) He, K.; Poole, C.; Mak, K. F.; Shan, J. *Nano Lett* **2013**, *13* (6), 2931–2936.
- (7) Li, T. *Phys. Rev. B* **2012**, *85* (23), 235407.
- (8) Wu, W.; Wang, L.; Li, Y.; Zhang, F.; Lin, L.; Niu, S.; Chenet, D.; Zhang, X.; Hao, Y.; Heinz, T. F.; Hone, J.; Wang, Z. L. *Nature* **2014**, *514* (7523), 470–474.
- (9) Zhu, H.; Wang, Y.; Xiao, J.; Liu, M.; Xiong, S.; Wong, Z. J.; Ye, Z.; Ye, Y.; Yin, X.; Zhang, X. *Nat. Nanotechnol.* **2015**, *10* (2), 151–155.
- (10) Feng, J.; Qian, X.; Huang, C.-W.; Li, J. *Nat. Photonics* **2012**, *6* (12), 866–872.